

Evidence of spatially selective refractive index modification in 15GeSe₂-45As₂Se₃-40PbSe glass ceramic through correlation of structure and optical property measurements for GRIN applications

Laura Sisken,^{1,*} Charmayne Smith,¹ Andrew Buff,¹ Myungkoo Kang,¹ Karima Chamma,¹ Peter Wachtel,² J. David Musgraves,² Clara Rivero-Baleine,³ Andrew Kirk,³ Matthew Kalinowski,¹ Megan Melvin,¹ Theresa S. Mayer,⁴ and Kathleen Richardson^{1,2}

¹CREOL, The College of Optics and Photonics, University of Central Florida, 4304 Scorpius St., Orlando FL 32816, USA

²IRradiance Glass, 3259 Progress Drive Orlando, FL 32826, USA

³Missiles and Fire Control, Lockheed Martin, 5600 Sand Lake Road Orlando, Florida 32819, USA

⁴Virginia Polytechnic Institute and State University, Blacksburg, VA 24061, USA

*sisken@knights.ucf.edu

Abstract: Thermally-induced nucleation and growth of secondary crystalline phases in a parent glass matrix results in the formation of a glass ceramic. Localized, spatial control of the number density and size of the crystal phases formed can yield ‘effective’ properties defined approximately by the local volume fraction of each phase present. With spatial control of crystal phase formation, the resulting optical nanocomposite exhibits gradients in physical properties including gradient refractive index (GRIN) profiles. Micro-structural changes quantified via Raman spectroscopy and X-ray diffraction have been correlated to calculated and measured refractive index modification verifying formation of an effective refractive index, n_{eff} , with the formation of nanocrystal phases created through thermal heat treatment in a multi-component chalcogenide glass. These findings have been used to define experimental laser irradiation conditions required to induce the conversion from glass to glass ceramic, verified using simulations to model the thermal profiles needed to substantiate the gradient in nanocrystal formation. Pre-nucleated glass underwent spatially varying nanocrystal growth using bandgap laser heating, where the laser beam’s thermal profile yielded a gradient in both resulting crystal phase formation and refractive index. The changes in the nanocomposite’s micro-Raman signature have been quantified and correlated to crystal phases formed, the material’s index change and the resulting GRIN profile. A flat, three-dimensional (3D) GRIN nanocomposite focusing element created through use of this approach, is demonstrated.

© 2017 Optical Society of America

OCIS codes: (110.2760) Gradient-index lenses; (160.2750) Glass and other amorphous materials; (300.6450) Spectroscopy, Raman; (110.3080) Infrared imaging.

References and links

1. O. M. Efimov, L. B. Glebov, L. N. Glebova, K. C. Richardson, and V. I. Smirnov, “High-efficiency Bragg gratings in photothermorefractive glass,” *Appl. Opt.* **38**(4), 619–627 (1999).
2. O. M. Efimov, L. B. Glebov, V. I. Smirnov, and L. Glebova, “Process for production of high efficiency volume diffractive elements in photo-thermo-refractive glass,” US 09/648,293, (2003).
3. L. G. Atkinson, D. S. Kindred, D. T. Moore, and J. R. Zinter, “Negative abbe number radial gradient index relay and use of same,” US 08/017,034 (1994).
4. T. H. Tomkinson, J. L. Bentley, M. K. Crawford, C. J. Harkrider, D. T. Moore, and J. L. Rouke, “Rigid endoscopic relay systems: a comparative study,” *Appl. Opt.* **35**(34), 6674–6683 (1996).

5. D. Gibson, S. Bayya, and J. Sanghera, Homogeneous and Gradient Index (GRIN) Materials For Multi-Band IR Optics” in Classical Optics 2014 (Optical Society of America, 2014).
6. D. Gibson, S. Bayya, J. Sanghera, V. Nguyen, D. Scribner, V. Maksimovic, J. Gill, A. Yi, J. Deegan, and B. Unger, “Layered chalcogenide glass structures for IR lenses” in SPIE **9070**, Infrared Technology and Applications XL (2014).
7. D. Gibson, S. Bayya, V. Nguyen, J. Sanghera, M. Kotov, R. Miklos, and C. McClain, “IR-GRIN optics for imaging,” in Proc. of SPIE **9822** (SPIE, 2016).
8. S. Novak, P. T. Lin, C. Li, C. Lumdee, J. Hu, A. Agarwal, P. G. Kik, W. Deng, and K. Richardson “Direct print of multilayer gradient refractive index chalcogenide glass coatings by electrospray,” ACS Appl. Materials and Interfaces, in press (2017).
9. K. Richardson, J. David Musgraves, P. Wachtel, C. Rivero-Baleine, and T. Mayer, “Method of Forming an Optical Device and Optical Apparatus,” U.S. Patent No. 9,340,446 (17 May 2016).
10. M. Dussauze, A. Lepicard, M. Bondu, V. Rodriguez, F. Adamietz, T. Cardinal, E. Fargin and K. Richardson, Device and Method for Inducing by Thermal Poling a Spatially Controlled Refractive Index Gradient Inside an Amorphous Inorganic Material,” European Patent application #EP16176689.4 (28 June 2016).
11. L. G. Atkinson, S. N. Houde-Walter, D. T. Moore, D. P. Ryan, and J. M. Stagaman, “Design of a gradient-index photographic objective,” Appl. Opt. **21**(6), 993–998 (1982).
12. V. Nguyen, S. Larouche, N. Landy, J. S. Lee, and D. R. Smith, “Quantitative comparison of gradient index and refractive lenses,” J. Opt. Soc. Am. A **29**(11), 2479–2497 (2012).
13. S. Houde-Walter and D. T. Moore, “Real-time index profile measurement during GRIN glass fabrication,” Appl. Opt. **27**(3), 508–515 (1988).
14. G. Beadie, J. S. Shirk, A. Rosenberg, P. A. Lane, E. Fleet, A. R. Kamdar, Y. Jin, M. Ponting, T. Kazmierczak, Y. Yang, A. Hiltner, and E. Baer, “Optical properties of a bio-inspired gradient refractive index polymer lens,” Opt. Express **16**(15), 11540–11547 (2008).
15. R. A. Flynn, E. F. Fleet, G. Beadie, and J. S. Shirk, “Achromatic GRIN singlet lens design,” Opt. Express **21**(4), 4970–4978 (2013).
16. Y. Jin, H. Tai, A. Hiltner, E. Baer, and J. S. Shirk, “New class of bioinspired lenses with a gradient refractive index,” J. Appl. Polym. Sci. **103**(3), 1834–1841 (2007).
17. M. A. Pickering, R. L. Taylor, and D. T. Moore, “Gradient infrared optical material prepared by a chemical vapor deposition process,” Appl. Opt. **25**(19), 3364–3372 (1986).
18. J. B. MacChesney, P. B. O’Connor, and H. M. Presby, “A new technique for the preparation of low-loss and graded-index optical fibers,” Proc. IEEE **62**(9), 1280–1281 (1974).
19. S. D. Campbell, D. E. Brocker, J. Nagar, and D. H. Werner, “SWaP reduction regimes in achromatic GRIN singlets,” Appl. Opt. **55**(13), 3594–3598 (2016).
20. L. Petit, N. Carlie, T. Anderson, J. Choi, M. Richardson, and K. C. Richardson, “Progress on the Photoresponse of Chalcogenide Glasses and Films to Near-Infrared Femtosecond Laser Irradiation: A Review,” IEEE J. Sel. Top. Quantum Electron. **14**(5), 1323–1334 (2008).
21. J. W. Chan, T. Huser, S. Risbud, and D. M. Krol, “Structural changes in fused silica after exposure to focused femtosecond laser pulses,” Opt. Lett. **26**(21), 1726–1728 (2001).
22. P. Němec, J. Jedelský, M. Frumar, M. Štábl, and M. Vlček, “Structure, thermally and optically induced effects in amorphous As₂Se₃ films prepared by pulsed laser deposition,” J. Phys. Chem. Solids **65**(7), 1253–1258 (2004).
23. K. Palanjyan, R. Vallee, and T. Galstian, “Photoinduced GRIN lens formation in chalcogenide Ge-As-S thin films,” in Proc. of SPIE **9288** (SPIE, 2014).
24. A. Saitoh and K. Tanaka, “Self-developing aspherical chalcogenide-glass microlenses for semiconductor lasers,” Appl. Phys. Lett. **83**(9), 1725–1727 (2003).
25. J. Choi, “Femtosecond laser written diffractive optical elements and their applications,” PhD Dissertation, College of Optics, the University of Central Florida (2010).
26. C. Ye and R. R. McLeod, “GRIN lens and lens array fabrication with diffusion-driven photopolymer,” Opt. Lett. **33**(22), 2575–2577 (2008).
27. A. K. Buff, “A Study of Crystallization Behavior in Phase Separated Chalcogenide Glasses,” MS Thesis, Department of Materials Science and Engineering, University of Central Florida (2016).
28. A. Yadav, M. Kang, C. Smith, J. Lonergan, A. Buff, L. Sisken, K. Chama, C. Blanco, J. Caraccio, T. Mayer, C. Rivero-Baleine, and K. Richardson, “Influence of phase-separation on structure-property relationships in the (GeSe₂-3As₂Se₃)_{1-x}PbSex glass system,” Physics and Chemistry of Glasses: European Journal of Glass Science and Technology Part B. (2017).
29. W. Holand and G. H. Beall, *Glass Ceramic Technology* (Wiley, 2012).
30. N. C. Anheier and H. A. Qiao, “A mid-infrared prism coupler for bulk and thin film optical analysis,” in Proc. of SPIE **8016** (SPIE, 2011).
31. H. A. Qiao, N. C. Anheier, J. D. Musgrave, K. Richardson, and D. W. Hewak, “Measurement of chalcogenide glass optical dispersion using a mid-infrared prism coupler” in Proc. of SPIE **8016** (SPIE, 2011).
32. H. A. Qiao, K. A. Lipschultz, N. C. Anheier, and J. S. McCloy, “Rapid assessment of mid-infrared refractive index anisotropy using a prism coupler: chemical vapor deposited ZnS,” Opt. Lett. **37**(9), 1403–1405 (2012).
33. N. Carlie, N. C. Anheier, Jr., H. A. Qiao, B. Bernacki, M. C. Phillips, L. Petit, J. D. Musgraves, and K. Richardson, “Measurement of the refractive index dispersion of As₂Se₃ bulk glass and thin films prior to and

- after laser irradiation and annealing using prism coupling in the near- and mid-infrared spectral range,” *Rev. Sci. Instrum.* **82**(5), 053103 (2011).
34. R. J. King and S. P. Talim, “A Comparison of Thin Film Measurement by Guided Waves, Ellipsometry and Reflectometry,” *Optica Acta: International Journal of Optics* **28**(8), 1107–1123 (1981).
 35. J. Woollam, B. Johs, C. Herzinger, R. Synowicki, and C. Bungay, “Optical Metrology,” *Critical Reviews of Optical Science and Technology* **CR72**, 3–28 (1999).
 36. S. Singh, “Refractive Index Measurement and its Applications,” *Phys. Scr.* **65**(2), 167–180 (2002).
 37. C. Saloma, V. Darla, and J. Muñoz, “Fourier transform refractometry using multichannel detection,” *Appl. Opt.* **32**(25), 4785–4789 (1993).
 38. P. Bon, G. Maucourt, B. Wattellier, and S. Monneret, “Quadriwave lateral shearing interferometry for quantitative phase microscopy of living cells,” *Opt. Express* **17**(15), 13080–13094 (2009).
 39. J. Yao, P. Meemon, M. Ponting, and J. P. Rolland, “Angular scan optical coherence tomography imaging and metrology of spherical gradient refractive index preforms,” *Opt. Express* **23**(5), 6428–6443 (2015).
 40. J. Yao, P. Meemon, and J. P. Rolland, “Nondestructive Metrology of Layered Polymeric GRIN Materials Using Optical Coherence Tomography” in *Imaging and Applied Optics Technical Papers* (Optical Society of America, 2012).
 41. J. Yao, J. Huang, P. Meemon, M. Ponting, and J. P. Rolland, “Simultaneous estimation of thickness and refractive index of layered gradient refractive index optics using a hybrid confocal-scan swept-source optical coherence tomography system,” *Opt. Express* **23**(23), 30149–30164 (2015).
 42. G. Yang, X. Zhang, J. Ren, Y. Yunxia, G. Chen, H. Ma, and J. L. Adam, “Glass Formation and Properties of Chalcogenides in a $\text{GeSe}_2\text{-As}_2\text{Se}_3\text{-PbSe}$ System,” *J. Am. Ceram. Soc.* **90**(5), 1500–1503 (2007).
 43. H. Wang, X. Zhang, G. Yang, Y. Xu, H. Ma, J. L. Adam, Z. Gu, and G. Chen, “Micro-crystallization of the infrared transmitting chalcogenide glass in $\text{GeSe}_2\text{-As}_2\text{Se}_3\text{-PbSe}$ system,” *Ceram. Int.* **35**(1), 83–86 (2009).
 44. B. Gleason, K. Richardson, L. Siskin, and C. Smith, “Refractive Index and Thermo-Optic Coefficients of Ge-As-Se Chalcogenide Glasses,” *Int. J. Appl. Glass Sci.* **7**(3), 374–383 (2016).
 45. A. Marotta, A. Buri, and F. Branda, “Nucleation in glass and differential thermal analysis,” *J. Mater. Sci.* **16**(2), 341–344 (1981).
 46. J. Massera, J. Remond, J. Musgraves, M. J. Davis, S. Mixture, L. Petit, and K. Richardson, “Nucleation and growth behavior of glasses in the $\text{TeO}_2\text{-Bi}_2\text{O}_3\text{-ZnO}$ glass system,” *J. Non-Cryst. Solids* **356**(52-54), 2947–2955 (2010).
 47. C. S. Ray and D. E. Day, “An Analysis of Nucleation-Rate Type of Curves in Glass as Determined by Differential Thermal Analysis,” *J. Am. Ceram. Soc.* **80**(12), 3100–3108 (1997).
 48. A. Zakery and S. R. Elliott, *Optical Nonlinearities in Chalcogenide Glasses and their Applications* (Springer, 2007).
 49. J. N. Zemel, J. D. Jensen, and R. B. Schoolar, “Electrical and Optical Properties of Epitaxial Films of PbS, PbSe, PbTe, and SnTe,” *Phys. Rev.* **140**(1A), A330–A342 (1965).
 50. L. Gampel and F. M. Johnson, “Index of Refraction of Single-Crystal Selenium,” *J. Opt. Soc. Am.* **59**(1), 72–73 (1969).
 51. B. Gleason, “Designing Optical Properties in Infrared Glass,” PhD dissertation, Department of Material Science and Engineering, Clemson University TigerPrints **1568**, (2015).
 52. R. P. Wang, A. Smith, A. Prasad, D. Y. Choi, and B. Luther-Davies, “Raman spectra of GexAsySe_{1-x-y} glasses,” *J. Appl. Phys.* **106**(4), 043520 (2009).
 53. J. Chen and W. Z. Shen, “Raman study of phonon modes and disorder effects in $\text{Pb}_{1-x}\text{Sr}_x\text{Se}$ alloys grown by molecular beam epitaxy,” *J. Appl. Phys.* **99**(1), 013513 (2006).
 54. R. Zallen, M. L. Slade, and A. T. Ward, “Lattice Vibrations and Interlayer Interactions in Crystalline As_2S_3 and As_2Se_3 ,” *Phys. Rev. B* **3**(12), 4257–4273 (1971).

1. Introduction

Gradient refractive index (GRIN) optics have been increasingly sought after to enhance optical system performance while reducing the number, size, and/or weight of the optical components needed in a system, while maintaining optical performance (size, weight, and power – SWaP). GRIN optical elements are well established for use in visible systems [1–4], but few approaches have been proposed for components in the mid- or long-wave infrared (IR) [5–10]. Current GRIN fabrication has been realized with ion-exchange [11–13], stacking and pressing layers of differing index in either glass or polymers [5–7, 14–16], and using chemical vapor deposition [17, 18]. These techniques often have limitations on the geometry of index profile possible, due to the fabrication technique (i.e., diffusion) and materials used.

There are many instances where an arbitrary profile within a GRIN element would allow further reduction of SWaP by allowing correction of multiple types of aberrations without the need for additional optical elements [19]. Laser-written structures created with a highly focused beam within a bulk optical material would allow fabrication of such an arbitrary

structure with fine precision on the order of microns. Typically, laser-written structures have an index change based on bonding modifications (expansion or contraction) [20–22] or extreme structural changes [1,2,23–26] where phase conversion (glass to crystalline) has been realized.

One structural change that can be created spatially and permanently in an optical glass is the controlled formation of nano-crystallites into a glassy matrix [27,28] yielding a glass ceramic (GC). Traditional glass ceramics are created through a two-step homogeneous heat treatment (HT) where the first step is a nucleation HT that creates crystal nuclei, and the second is a growth HT that grows the nuclei into larger crystals [29]. The resulting composite material has material properties that are intermediate to those of the parent glass and the precipitated crystal phase(s), and are defined by the resulting volume fraction (size, shape and number density) of each phase present. For optical GCs, the impact of the secondary phase on the scatter and absorption are highly important. Since the two phases generally have different refractive indices, there is inherent scatter in the material if the secondary phase is on the order of the wavelength range of use, or larger. Also, induced absorption of the crystalline species in the spectral regime of interest could be problematic for certain applications if the phase is anisotropic and/or induces stress birefringence.

Once a GRIN element is created its resulting index profile must be validated with sub- μm spatial accuracy in order to ensure that the method used to create the GRIN was correct. Traditional, *absolute* refractive index measurement methods include prism coupling [30–33], spectroscopic ellipsometry [34,35], minimum deviation [36], and Sagnac interferometry [37]. These techniques are often not suitable for measuring fine gradients in refractive index, since they typically measure over spatial areas in the mm to cm range. *Relative* refractive index measurements can be measured interferometrically [13], but these measurements are averages throughout the entire volume of the sample, making it difficult to realize subtle, spatially varying changes. Commercial interferometry systems, such as the Phasics SID4bio, have been developed as metrology tools for step-index preforms and can evaluate resulting index profile through quadri-wave lateral shearing interferometry on a visible microscope with up to diffraction limited resolution depending on the microscope conditions used [38]. Optical coherence tomography (OCT) has also been used to measure GRIN structures in polymer stacks, however the technique requires GRIN structures that are discontinuous in order to get back reflections at the interfaces [39–41]. While used extensively in the visible region, many of these methods have not been extended for use/demonstrated in the IR.

Several *indirect* measurements have also been created in order to quantify GRIN structures. One such method uses micro-FTIR measurements in polymer systems to determine the ratios of different polymer materials present at a given spatial location [16]. This method is able to quantify the effective index of the material at a given surface location, and with cutting and polishing of a sample, the entire GRIN profile could be mapped out. This technique though is only useful for systems that include multiple materials with distinct FTIR spectra, and is time-consuming and sensitive to sample quality during fabrication. Additionally, image analysis [6], system performance [6,14], and wave-front sensing [23] can be used to verify that a GRIN element works the way it was designed to; however, this approach does not fundamentally allow one to know the actual index profile of the resulting component, rather it only quantifies its optical performance in a system.

We have developed an indirect measurement approach aimed at providing a method of correlating index to structural changes in the formation of an optical glass ceramic. Discussed herein, it employs micro-Raman spectroscopy which can give structural selectivity combined with the spatial control of a microscopic measurement. This technique has the potential to be well suited for glass-ceramic systems since it can probe the fine structural changes that develop upon the early stages of conversion of glass networks when traditional tools cannot easily detect nucleation, through the steps of crystal growth inside the glassy matrix. This approach is amenable to spatial mapping strategies in both radial (x-y) and axial (z, through

material removal) directions allowing true three-dimensional (3D) metrology of structural changes.

A nanocomposite chalcogenide glass ceramic GRIN structure has been manufactured through laser-induced ceramization of the parent glass. Conversion of glass to glass ceramic was realized by inducing homogeneous nucleation (nucleation without the use of nucleation agents). Growth of nuclei was realized using furnace growth, or using an absorbing, bandgap laser source which induced heating of crystal nuclei, already present inside of a glass. The intensity profile of the Gaussian laser beam translated into a gradient heat profile which varied spatially, and therefore created a gradient of crystal growth rate. The resulting spatially varying nanostructure (parent glass + precipitated nanocrystalline phases) resulted in a GRIN profile, where the effective index of the composite has been controlled by the local volume fraction of each of these phases present. The parent glass composition, $15\text{GeSe}_2\text{-}45\text{As}_2\text{Se}_3\text{-}40\text{PbSe}$ (154540 GAP-Se) has been evaluated in its base form, following a homogeneous (furnace) nucleation HT, and then following growth with (i.) a homogeneous furnace growth HT or (ii.) through use of a Gaussian laser heating HT. Through this comparison, samples were examined to determine if analysis of a localized micro-Raman signature would prove viable for indirectly measuring the phase and refractive index evolution of a two-step cerammed material in a spatially selective way. Samples with two-step (nucleation plus growth) homogeneous HT had their refractive index, XRD, and Raman spectrum measured in order to determine if the growth of crystallites created an index change that could then be correlated with a change in the Raman spectra. A second sample then was put through a homogeneous furnace nucleation HT, and was subsequently grown with a Gaussian laser beam thermal profile, in order to spatially vary the growth of nanocrystals. Thus the laser HT profile, the crystal growth profile and resulting GRIN profile could then be compared. Lastly, the measured Raman spectra of a 2D cross-section of the laser-grown sample was compared to the two-step furnace HT samples to probe the spatial index profile of the sample. With this approach the Raman spectra could be mapped to a temperature profile that was compared to the thermal modeling of the laser irradiation condition in order to validate the model. The resulting sample was evaluated for optical functionality as a secondary confirmation that the gradient HT profile resulted in an index change in the material.

2. Experimental

2.1 Base glass properties

The material used in this study was $15\text{GeSe}_2\text{-}45\text{As}_2\text{Se}_3\text{-}40\text{PbSe}$ (154540 GAP-Se), a high lead-containing multicomponent glass discussed further in a recent publication [28]. This glass is near the boundary of the glass-forming region in the $\text{GeSe}_2\text{-As}_2\text{Se}_3\text{-PbSe}$ as discussed in [42,43] as depicted in the ternary phase diagram shown in Fig. 1(a). The high Pb content of this glass was deliberately chosen with the goal of increasing the amount of Pb-containing crystalline phases on crystallization to maximize the potential refractive index changes, Δn , in formation of a glass ceramic. The glass' physical properties and morphology are discussed in detail, along with other glasses in the $(\text{GeSe}_2\text{-}3\text{As}_2\text{Se}_3)_{1-x}\text{PbSe}_x$ series ($x = 0\text{-}55$ mol%), in [28].

Bulk glass was prepared by traditional melt/quench protocols using 5N pure elemental starting materials in 350 or 400g batches using procedures discussed in [27]. As-melted compositional uniformity to target batched composition was confirmed by Energy Dispersive X-ray Spectroscopy (EDS) using a Zeiss ULTRA-55 FEG SEM to confirm no variation between batch sizes. Starting materials were weighed and batched into 30 mm inner diameter quartz ampoules which were sealed using a gas-oxygen torch. The glass was melted at 700°C , quenched at 470°C and annealed at 170°C to minimize residual stresses in the melt. The resulting 30 mm diameter rod was sliced into approximately 2 mm thick plano blanks which were ground and polished, with a final $0.05\ \mu\text{m}$ slurry to yield blanks with an inspection polished surface shown in Fig. 1(b). Typical root mean square (rms) surface roughness of the

post-polished glass was 18 ± 6 nm. Surfaces were cleaned with acetone prior to irradiation to remove any dust or residue which could modify the glass' surface absorption behavior.

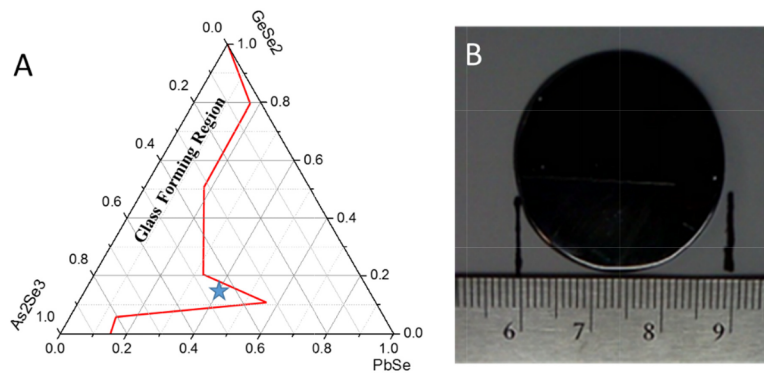


Fig. 1. (A) The glass forming region (to the left of the red line shown) as described by Wang and Yang et al. [42,43], in the As_2Se_3 - GeSe_2 - PbSe ternary system. The 15 GeSe_2 -45 As_2Se_3 -40 PbSe [154540 GAP-Se] composition is shown by the blue star. (B) A picture of a 30 mm polished slice of this glass in the visible.

Thermal conductivity and heat capacity were measured with a Thermtest TPS 2200 instrument to ascertain key thermal property attributes required for determining experimental conditions and as input for theoretical calculations. Where appropriate, the values of these properties measured at $T = 190^\circ\text{C}$ were used. Density was measured using the Archimedes principle at room temperature (RT) with an immersion fluid of deionized water with an AE Adams PGW Balance. Thermal expansion measurements were performed on a TA Instruments TMA 2940 thermo-mechanical analyzer on a $15 \times 2 \times 2$ mm rod. Thermal expansion in conjunction with the density at 20°C were used to estimate the density of the material at higher temperatures, specifically 190°C were needed. This correction resulted in a density change of 1%.

X-ray diffraction (XRD) measurements were performed on a PANalytical Empyrean, X-ray diffraction system with 1.8kW, $\lambda_{\text{CuK}\alpha} = 0.15418$ nm, and 40 mA, on bulk samples at RT to confirm lack of crystallinity in the as-melted glass. The refractive index was measured using a Metricon prism coupler that has been modified for use in the IR, and has been described elsewhere [30-33,44]. Measurements were made at $4.515 \mu\text{m}$ and 30°C . This technique measures over an approximately 2 mm diameter spot size. Raman measurements were performed at RT with a Bruker Senterra system with an excitation wavelength of 785 nm, 1 mW of power, a 20x objective, and 2.25 min exposure times. The spot size of the Raman laser at the sample's surface is approximately $2 \mu\text{m}$ with this objective. The exposure conditions were tested to make sure they were not inducing modifications by measuring multiple times in the same location on a test sample. Transmission was measured using a ThermoFisher Nicolet iS5 FTIR spectrometer and a CARY 500 UV-VIS spectrophotometer to cover the full wavelength range needed. Spectra were not corrected for Fresnel loss.

2.2 Furnace ceramization

Samples were fabricated using protocols discussed above and cut into numerous samples for furnace-based nucleation and growth HT. A schematic of the sectioning process used on samples for nucleation or nucleation and growth treatments are shown in Fig. 2 (left). Nucleation-like (I) and growth-like (U) curves were determined for this material in previous work [27] using the methods described in detail in [45-47]. These data were used to define nucleation and growth temperatures for homogeneous HT ceramization in a furnace, and to define the target temperatures required for laser-heating for laser-induced growth steps used.

I-U curves for the 154540 GAP-Se glass used here, and are shown in Fig. 2 (right). These curves do not provide absolute nucleation or growth rates, but rather show relative rates which are adequate for the objectives of this study.

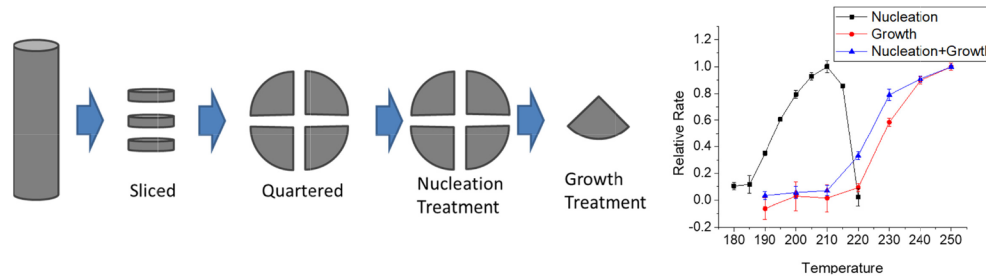


Fig. 2. (Left) Sample sectioning protocol: a rod was sliced into disks, which were then quartered. All of the quarters of one slice were then HT at a single nucleation temperature. Each of the quarters were then grown at a different growth HT temperatures. (Right) Nucleation-like (I) and growth-like (U) curve for the base 154540 GAP-Se glass [27]. When the sample goes through a nucleation step before growth, the growth curve shifts to lower values.

Heat treatments were performed in a ThermoScientific 48000 muffle furnace. The furnace was pre-heated to the desired temperature and equilibrated at the soak HT temperature for 30 min prior to introduction of samples. Samples were then placed inside of the furnace quickly to minimize the time the door was open in order to maximize the time the sample was at the desired temperature. The nucleation time used in this study was 2 hrs, and the growth time was 30 min for all samples. Two different nucleation temperatures were used on two separate slices, 190 and 200°C, and an additional slice underwent a growth HT without a nucleation treatment. Following nucleation, these slices were quartered and subjected to a specific growth HT of either 200, 210, 220, or 230°C. The XRD, refractive index, and Raman spectrum were measured for the post-furnace HT samples and compared to those of the starting base material.

X-ray diffraction (XRD) was used to identify the crystals that precipitated during the ceramization process. By looking at the intensities of the peaks with respect to XRD scans taken of the individual crystallites under the same XRD conditions, volume fractions of the different crystals were estimated. With these volume fractions and known refractive indices of the crystals [48–50], the effective refractive index, n_{eff} , for the post-HT'd samples were calculated by weighting the refractive index of each phase with its respective volume fraction present. This data was then compared to the measured refractive index values to show that the index change seen was from induced crystallites in the glassy matrix. Changes in the Raman spectrum upon HT were quantized and compared to the measured refractive index values in order to correlate the two measurement techniques.

2.3 Laser ceramization

Laser exposure with bandgap laser light was used to HT post-nucleated samples to allow for comparison of resulting structural properties with the furnace-only HT'd glass ceramics. In order to define laser conditions needed for suitable growth temperatures, theoretical calculations of laser-induced heating of 154540 GAP-Se glass were performed based on the measured base glass thermal properties at 190°C.

All laser irradiations were performed with a 532 nm, Spectra-Physics Millennia VS, CW laser in order to spatially vary the extent of crystal growth across an area defined by the laser beam's intensity profile. As the irradiation wavelength is well below the optical bandedge of the material, it can therefore be approximated as a surface heat source which induces a temperature profile throughout the volume of the (thin) sample. The sample for this experiment was pre-nucleated at 190°C for 2 hrs, as in the previous homogeneous furnace HT

experiments. The laser-induced heating profile was used to promote crystal growth during a 30 min exposure step, again consistent with protocol used in the previous experiment.

2.3.1 Simulations

Simulations were used to determine appropriate 532 nm irradiation conditions where the temperature profile in the sample would have (i) a peak temperature of 230°C in the sample's top center to promote high crystal growth, and (ii) a temperature of 190°C on the back surface and edges, where according to I-U curve data, and corroborated with measurements from nucleated samples, little to no crystal growth would occur. Simulations of laser-induced heating were performed with COMSOL Multiphysics using Eq. (1), as a surface heat source for a 2D-axially symmetric regime where Q_{in} is the heat source, P is the laser power, R is the reflection coefficient, r is the distance from the center of the irradiated area, and w_0 is the Gaussian beam waist. The input parameters for material properties used for the simulation were taken from the base glass measurements above. The reflection coefficient used was 0.26.

$$Q_{in} = P(1 - R) \left(\frac{2}{w_0^2} \right) e^{-\left(\frac{2r^2}{w_0^2} \right)} \quad (1)$$

In the simulations the beam waist and average power of the laser were varied. It was determined that the desired temperature profile conditions listed above could not be reached with the laser source alone serving as the heat source with the sample at room temperature. The desired 40°C temperature spread from the center of the sample's surface, to the edges of the sample with a peak temperature around 40°C was realized with the addition of an external temperature of 190°C. This external temperature was deemed acceptable, since it was the same as the nucleation temperature used on the sample and should not contribute to additional growth. While further (small levels) of nucleation might occur in the pre-nucleated sample over the growth period (30 mins), this was considered negligible. An added advantage to elevating the sample temperature before irradiation is that it decreased the probability of thermal shock and breakage of the sample, since a lower temperature gradient across the sample existed at the onset of the exposure. The external temperature, beam waist, and beam power conditions from the simulation were then used to define the experimental conditions used.

2.3.2 Experiment

The external temperature needed for the irradiation was applied by performing the irradiation through the outlet vent at the top of the same box muffle furnace used in section 2.1. The pre-nucleated (190°C for 2 hrs) sample was irradiated using a collimated beam waist of 10 mm and an average power of 0.89 W.

After irradiation, the 532 nm exposed sample was cross-sectioned through the middle, and Raman spectra were measured along the x-z plane of the glass sample to evaluate the change in the glass structure following the two-step process. Here the goal was to correlate the extent of conversion of glass to glass ceramic to structural modification, and therefore refractive index changes, imparted through the formation of nanocrystals. The multiple measurement points through the exposed sample are depicted in Fig. 3. Data points were taken at a spacing of 1 mm in the x-direction and 0.25 mm in the z-direction using the same conditions and spatial resolution as in section 2.1.

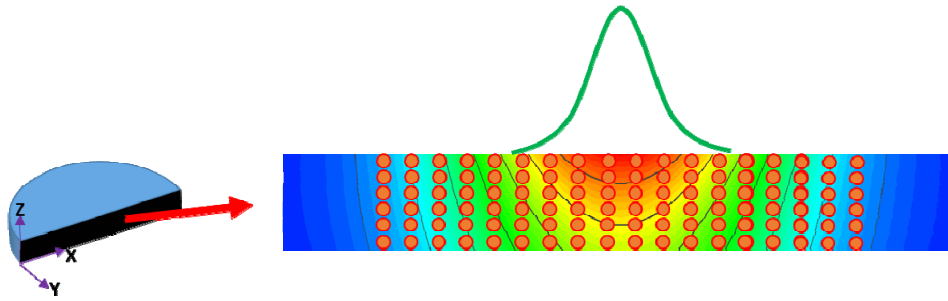


Fig. 3. Raman spectra were measured at 0.25 mm increments in the z-direction, and 1 mm in the x-direction (depicted by red dots, and is not to scale) on a cross-sectioned disk to quantify the extent of the modifications across the 2D sample volume. The background coloration (not to scale) is representative of the expected temperature profile while the sample is irradiated, while held at 190°C. The green, Gaussian shaped “beam” incident on the top surface is representative of the beam size with respect to the sample diameter, with a Gaussian intensity profile depicted on the sample surface.

The resulting spatially varying Raman measurements were then converted to the structure-defined temperature scale obtained from Raman measurements of furnace-only heat treated samples. The resulting temperature profiles were compared to those predicted by the thermal models for agreement. Using the Raman-to-index correlation (see Fig. 6(c)) the experimentally measured Raman data were converted into refractive index, and using the refractive index data at different HT temperatures the simulated temperature profile was converted to index to see how slight changes in thermal history would affect the index profile.

Lastly, to validate the assumption that the gradient growth profile imparted by the laser heating method resulted in an effective index profile with optical function (focusing), a collimated 2 μm laser was propagated through the irradiated portion of the sample before it was sectioned, and the beam profile after the sample was measured. Measurements were made at multiple distances in order to determine if any focusing of the beam could be observed with a Spiricon Inc. Pyrocam III.

3. Results and discussion

3.1 Base glass properties

As discussed in [27,28] the base 40 mol% PbSe GAP-Se glass used in the present study exhibits liquid-liquid phase separation (LLPS). The result of this morphological compositional non-uniformity has been shown to affect physical and optical properties of the as-melted glass [27,28], as well as its post-HT'd properties [27] upon furnace HT to form an optical nanocomposite. The as-melted glass exhibits two amorphous phases with compositions of phases quite dissimilar from the Ge:As:Pb:Se ratios of the as-batched compositions. These attributes are described in [27]. Specifically, the 154540 GAP-Se composition exhibits Pb-deficient droplets in a Pb-rich matrix, and it is believed that when crystallization occurs, it occurs in the higher Pb-containing matrix, as the glass' stability ($\Delta T = T_x - T_g$) is reduced with the high Pb content.

The thermal properties of the base glass used in the numerical simulations used to predict laser induced heating and corresponding thermally induced structure and property changes are summarized in Table 1. Note that in addition to ambient temperature data, values were measured where possible, at the extremes of the elevated temperature range used for processing. Additional material properties including T_g , hardness, and CTE as a function of PbSe content and melting protocol can be found in [27,28].

Table 1. Thermal properties for 15As₂Se₃-45GeSe₂-40PbSe that were used in simulations.

Temperature (°C)	<i>k</i> (W/mK)	<i>C_p</i> (J/g•K)	<i>ρ</i> (g/cm ³)
25	0.239 ± 0.003	0.229 ± 0.006	5.48
50	0.249 ± 0.002	0.228 ± 0.002	5.47*
100	0.263 ± 0.002	0.238 ± 0.008	5.45*
190	0.309 ± 0.004	0.232 ± 0.029	5.42*
230	0.321 ± 0.004	0.251 ± 0.012	5.39*

*data estimated from measured thermal expansion data

The XRD spectrum of the base glass shows two amorphous humps as seen in Fig. 4(a) which confirms that the sample is X-ray amorphous and void of any crystalline phase before HT.

The refractive index of the base glass measured at 30°C and a wavelength of 4.515μm is 3.0460, and the within-slice index uniformity was mapped across one of the 30 mm diameter samples. This map, shown in Fig. 4(b) illustrates good refractive index uniformity with a standard deviation of 0.0004. The sensitivity of the measurement technique [44,51] is 0.0005 for absolute index measurements; thus, the standard deviation across the sample is within the error of the measurement.

Transmission for the base glass is seen in Fig. 4(c). The absorption value listed in Table 2 is the estimated absorption coefficient and, in reality, is likely actually higher since the transmission value is at the edge of the sensitivity of the measurement system.

The Raman spectrum of the base glass consists of several broad bands associated with network constituents, as seen in the left portion of Fig. 4(d) below. The peak near 200 cm⁻¹ is attributable to the GeSe_{4/2} units, while the broad peak around 246 cm⁻¹ can be broken down into several peaks associated with AsSe_{3/2} at 225 cm⁻¹ and 240 cm⁻¹ [28,51,52]. Additionally, Se-Se presents a contribution to the main band's shoulder around 250 cm⁻¹ [51,52]. The Raman spectra are similar to those observed in Pb-free Ge-As-Se glasses that are past stoichiometry with respect to As₄₀Se₆₀, with small amounts of Ge added into the glass network [51,52]. Since Ge and Pb are both 4-fold coordinated, it is consistent that As-Se features would be minimally affected if Pb substitutes into a Ge site, and would explain why there is a lower frequency Ge-Se feature at 200 cm⁻¹ than Ge-As-Se glasses with a similar As-Se ratio [51,52].

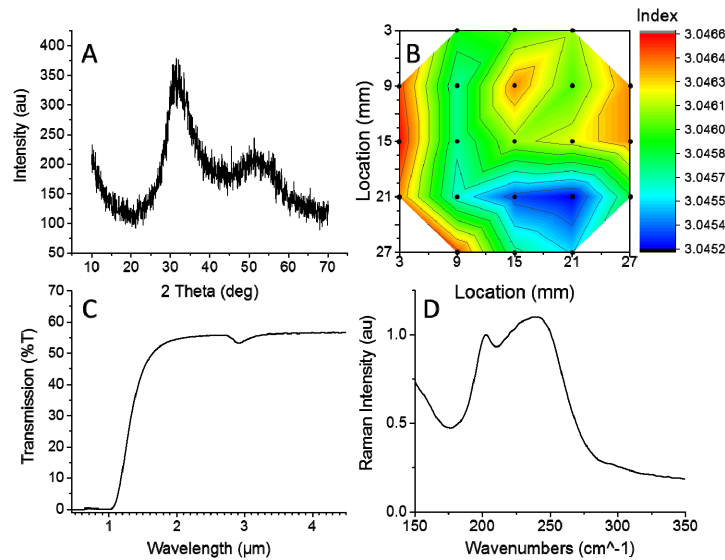


Fig. 4. (A) XRD spectrum for the base glass confirming the glass' as-melted x-ray amorphous nature. (B) 2-D within-slice refractive index homogeneity map ($\lambda = 4.515\mu\text{m}$) measured at 21 locations across the 30 mm diameter slice. The dots show measurement locations and the spot size of the measurement was ~ 2 mm. The color variation shows the range of index variation (C) Transmission spectrum for a 2 mm thick sample, not corrected for Fresnel loss. (D) MicroRaman spectra of the base glass ($\lambda_{\text{exc}} = 785\text{nm}$).

Table 2. The base glass optical properties of the melt prior to irradiation and/or HT. The index value is the average of the measurements used in Fig. 4(b), and the error is the standard deviation of these measurements.

Property Pre-exposure	Value
Absorption	$> 65.7 \text{ cm}^{-1}$ (532 nm)
Index	3.0460 ± 0.0004 ($\lambda = 4.515 \mu\text{m}$, 30°C)

3.2 Property modification from a two-step thermal (furnace only) heat treatment

Based on the I-U curves in Fig. 2 [27], nucleation and growth temperatures were chosen for the furnace only HT conditions. Due to a partial overlap in the I-U curves, nucleation temperatures were chosen to be below the peak nucleation temperature, at 190 and 200°C so that there would not be any crystal growth occurring while the sample was being nucleated. This allows for more controlled and uniform crystal growth in order to decrease induced scatter. Growth temperatures were chosen to be in the range of 200-230°C, in order to be able to evaluate where the onset of measurable crystallization occurs in the glass, as the growth curve shifts to lower HT temperatures after nucleation.

XRD was measured on the samples to see the evolution of the growth of a crystal phase/phases with the different HT protocols performed. The spectra for the 190°C nucleation step plus the various growth temperatures ($t = 30$ min) are shown in Fig. 5(a) below, and is representative of the different spectra seen. The crystal phases seen for this type of glass were previously identified in [27] and found to be As_2Se_3 , PbSe, and Se, with the first two being the dominant phases. The increase in the peaks at 2θ values of 22° (Se), $31\text{-}33^\circ$ (PbSe, As_2Se_3 , Se), 44° (PbSe), and 53° (As_2Se_3) confirms that these crystal phases are precipitating out of the glassy matrix upon HT. Additionally, in all the samples the same crystal peaks were seen to emerge concurrently, suggesting there are no phase-specific thermal conditions for the appearance of any of the crystal phases being formed for the specified HT conditions.

The refractive index of the post-HT'd glass was then measured with a prism coupler on these samples, and is plotted as a function of HT temperature in Fig. 5(b). As can be seen,

there is an initial small increase in index with increase in HT temperature, a further increase in slope at middle temperatures, and a leveling off of index increase for high growth temperatures. This would be indicative of low crystallization rates at low temperatures and a maximum amount of conversion at high temperature. The plateau seen at high temperature also suggests a depletion in the constituents available to participate in the crystallization following 30 mins at the highest growth temperatures shown. Additionally, more index change is seen at lower growth temperatures for higher nucleation temperatures, supporting our belief that a higher number density of nuclei is formed, consistent with the nucleation rate data in the I-U curves.

The measured refractive index was then plotted against the computed effective index obtained from estimates of volume fractions of phases seen in XRD spectra in Fig. 5(c), showing excellent agreement. Note that this correlation holds for each of the nucleation conditions used. This correlation allows us to definitively correlate the XRD phase formation to the observed effective refractive index change and to also associate it directly to the crystallization process in the glass ceramic's formation process.

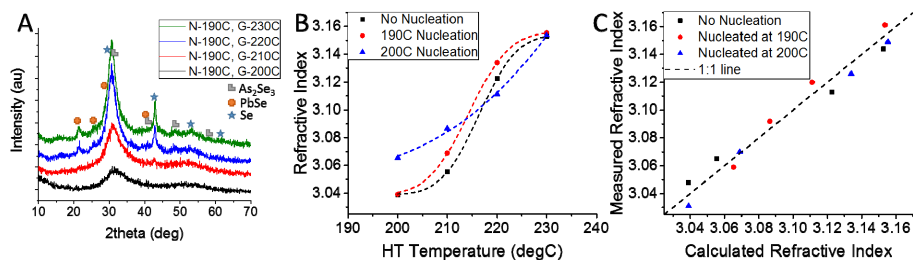


Fig. 5. (A) Representative XRD spectra for the 154540 GAP-Se glass following nucleation at 190°C, with furnace HT at temperatures shown for 30 min. (B) Measured refractive index ($\lambda = 4.515 \mu\text{m}$) versus growth temperature for various nucleation temperatures. (C) Measured (experimental) refractive index values obtained as a function of HT temperature, as compared to calculated refractive index based on volume fraction of crystal phase formed from XRD spectra.

The Raman spectra of the furnace HT samples were also measured and compared to those of the base glasses prior to HT. A representative plot showing the general trend with HT for one set of nucleation temperature samples (190°C) is seen in Fig. 6(a). Since PbSe has dominant peaks observed at 143 and 243 cm^{-1} [53] and As₂Se₃ has multiple peaks between 145 and 273 cm^{-1} [54], no evidence of crystallinity can be seen in the Raman data. This may be due to the low Raman cross section of the precipitated phase, low volume fraction of nanocrystallites that are overshadowed by the remaining glassy matrix, or the crystals that formed were mixed or were not Raman active. We know however, that XRD has confirmed that the crystals shown in Fig. 5(a) are present in the material under these treatment conditions.

While distinct crystal peaks are not seen in the Raman spectra, a systematic and reproducible decrease in the peak around 246 cm^{-1} is observed with heat treatment. The spectral region from 220 to 250 cm^{-1} contains numerous bands related to various As-Se vibrations. In order to characterize a potential “extent of conversion towards crystallization” from the Raman data, we define a Raman ratio to track such changes. We define our Raman ratio as the ratio in peak intensity between the peak at $\sim 200 \text{ cm}^{-1}$ and the peak at 246 cm^{-1} . In the Fig. 6(a) we have normalized peak Raman intensity at 200 cm^{-1} to allow for easy visualization of the changes in the As-Se dominant peak at 246 cm^{-1} . Using the Raman peak identifications from section 3.1, an increase is seen in the ratio of Ge-Se to As-Se features, which is believed to be associated with the conversion of the amorphous network's As-Se bonds towards the resulting observed (via XRD) As₂Se₃ crystalline configuration. Since the

dominant two crystal phases identified by XRD are As_2Se_3 and PbSe , the formation of crystalline As_2Se_3 associated with the conversion of glass to nanocrystallite-containing glass ceramic, would likely cause a change/decrease in the glass' As-Se bands, and the PbSe would not affect either band structure. We propose to use this Raman ratio as a correlative tool to allow comparison on spatially varying 'conversion' associated with formation of high refractive index nano-crystals precipitated in both furnace and laser-induced growth HT.

From Fig. 6(b) below, a trend can be seen in the shape of the Raman ratio versus HT temperature plot for glasses nucleated at the temperatures shown. The ratio trend has a similar shape to the index versus HT plot in Fig. 5(b), where there is little change between points at lower and higher temperatures. One can also observe a shift in the onset of crystallization observed for higher nucleation temperatures, which is consistent with the I-U curve in Fig. 2 and the index versus HT plot in Fig. 5(b). This is again consistent with our belief that a higher number density of nuclei are formed at higher nucleation temperatures based on the higher nucleation rate data seen in the I-U curves.

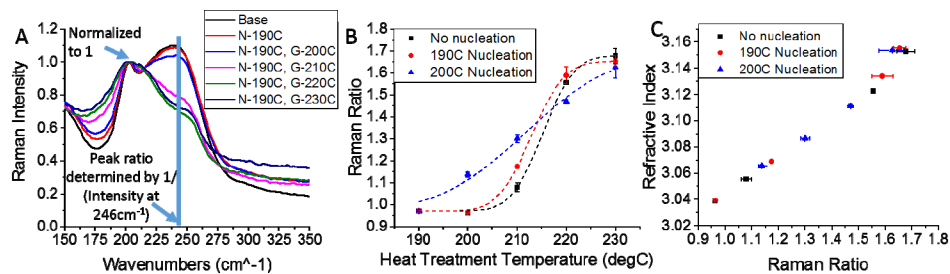


Fig. 6. (A) Raman spectra at $\lambda_{exc} = 785\text{nm}$ for base glass prior to and following nucleation (190°C) and growth treatments. Spectra have been normalized to the 200 cm^{-1} peak. (B) Raman ratio versus heat treatment temperature for various nucleation protocols. (C) Direct correlation between Raman ratio and refractive index indicative of fractional conversion of glass to glass ceramic.

Figure 6(c) shows a plot of the Raman ratio versus refractive index, and includes data for all nucleated and grown samples and illustrates excellent correlation between the Raman ratio with measurable change in refractive index. This correlation directly supports our hypothesis that the conversion of $\text{AsSe}_{3/2}$ units related to the decrease in the 246 cm^{-1} band is directly correlated to formation of As_2Se_3 crystals as suggested by the XRD data. The linear trend is seen to exist between the refractive index and Raman up to a ratio of approximately 1.6, regardless of the nucleation condition, suggesting that while the process may have a kinetic/rate dependence, the mechanism of conversion is the same.

Since we have now correlated the XRD-defined phase formation with a Raman spectral signature, and therefore, the effective refractive index with the Raman data, it should follow that these data can be used in furthering our understanding of the temperatures required to induce specific changes in refractive indices. Here, we use the thermal data extracted from the Raman ratio plots to serve as input for confirmation of our heat flow model within the glass. This model is important in our definition of laser irradiation conditions necessary to give specific induced refractive index modification through the use of a gradient heat source, our Gaussian shaped laser beam.

3.3 Property modification following bandgap laser irradiation

The Raman spectra measured on the cross-section of the irradiated sample shown in Fig. 3 were used to calculate a Raman ratio for each location. As depicted in the image, it was expected that the edges of the sample would have no Raman change and were therefore not measured. These data for the Raman ratio were used to solve for the expected temperature that was seen at each location using the fitted curve seen in Fig. 6(b). This temperature map

was then compared to the simulated temperature profile calculated based on laser parameters and material thermal properties. Both profiles are compared in Fig. 7.

The two profiles show correlation, which validates that to first order, we have adequately captured key property inputs and system attributes in our model. This also supports our link to assessing and defining a laser-induced growth temperature profile for our glass, albeit in a highly absorbing regime. This suggests that we can induce not only spatially varying heating but also conversion towards crystallization and index change for precipitation of high index nanocrystals. A possible source of discrepancy or error in our analysis is that the sample may have not been sliced exactly through the center of the irradiated region, leading to the temperatures seen in the cross-sectioned region being more concentrated than the simulations. Additionally, as our Raman ratio determination and material properties were measured on multiple samples taken from two large melts with possible minor variations in thermal history and as-melted structures, very small sample to sample variation, may be present. Lastly, while our model considered the expected temperature profile in the sample using material properties measured at 190°C, a portion of the sample experienced a higher temperature ($T_{\max} \sim 230^\circ\text{C}$) during irradiation. As shown in Table 1 the higher thermal property data (and lower density value) for this target temperature (230°C) would be expected to modify the heat transfer behavior in the irradiated region. This, in the absence of a direct measurement of the heat transfer coefficient used for convective heat flux at the boundary (not been measured for this material) is likely contributing to an offset in the magnitude and spatial variation in our simulated temperature profile.

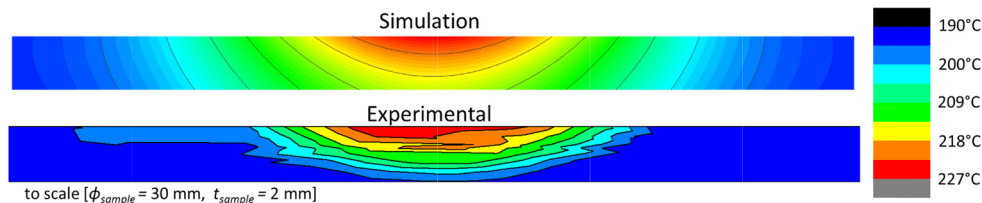


Fig. 7. (Top) Simulated temperature profile induced for the $\lambda = 532$ nm laser irradiation conditions used, incorporating thermal properties measured on the bulk glass. (Bottom) The experimentally predicted temperature profile as determined by the change in the Raman ratio with temperature.

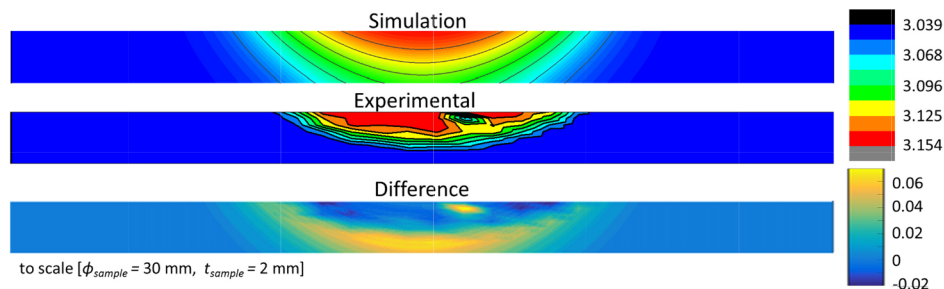


Fig. 8. The mapped refractive index values predicted by simulation (top) and prediction from the experimentally measured Raman (middle). The bottom plot is the difference between the two spectra in refractive index units.

A similar approach was then employed to predict the expected refractive index gradient that would result from the said thermal profile induced by the laser growth protocol used. Here, the Raman ratio at each point was converted into a spatially varying refractive index profile using the fitted line of the Raman versus index plot in Fig. 6(c). The simulated temperature profile was converted to a refractive index map using the fitted line of the refractive index versus temperature plot, shown in Fig. 5(b). Here, the two spatial maps show

less agreement, specifically in the axial (z) direction as seen in Fig. 8. The simulated index profile predicted exhibits a slightly lower peak index, and covers a larger area and depth than realized in the measured data as can be seen in Fig. 8 (bottom) where the simulated index profile is subtracted from the experimental profile to quantify the difference spatially between the two profiles. This variation may be attributed again to the same issues seen with the temperature plot such as the unknown heat transfer coefficient in the center of the irradiated region, a slight variation in crystallization between melts, and potential deviations of the model inputs from the true material properties at temperature.

As this related index profile represents a coarse but clearly defined three dimensional gradient resembling a flat lens design, the post-laser grown sample was evaluated for optical functionality. Specifically, the post-irradiated sample was tested for its ability to focus light before it was sectioned in half for the Raman measurement. To probe if the resulting part's index modification yielded focusing, a $\lambda = 2 \mu\text{m}$ collimated laser beam was transmitted through the irradiated region and the size of the beam waist was measured at various location to make a coarse estimation of a calculated focal length. While somewhat irregular, a clearly defined focus spot was observed and quantified for this first attempt at a 3-D GRIN element, and is seen in Fig. 9. Based on measurements shown where the position of the detector without and then with sample in place is moved, a focal length was able to be calculated. For the refractive index profile induced by the nucleation and (laser-induced) growth protocol used here, a flat, GRIN lens with a focal length of $84 \pm 3 \text{ mm}$ was demonstrated. The post-processed lens region was inspected for surface modification. Laser exposure and HT resulted in a slight bulge in the exposed region (radius of curvature measured to be $1400 \pm 30 \text{ mm}$ as quantified by white light interferometry) which was not removed (polished) prior to measurement. As can be seen, this minor deviation to the planar surface could not have resulted in the measured focus seen at 84 mm . This confirms the viability of our approach to create a laser-induced, spatially variable glass ceramic nanocomposite, for GRIN element production.

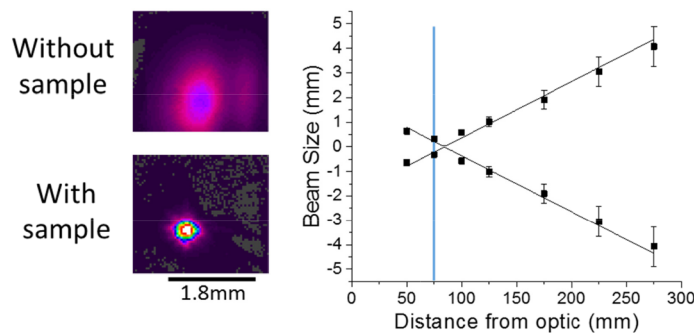


Fig. 9. Focal spot as measured in a laser-written 3-D GRIN structure. (Left) focal spot of measurement beam (collimated $2\mu\text{m}$ laser) without and with sample inserted, where the color scale shows the center beam intensity (yellow high, purple low). (Right) beam waist measurement as a function of position, and fitted (solid line) to extrapolate the measured focal length of the GRIN lens $84.3 \pm 2.7 \text{ mm}$. The blue line represents the plane where the images on the left were taken.

4. Conclusion

This paper examines the structural evolution of a multicomponent infrared glass as it is converted to an optical nanocomposite through both two-step furnace HT, a furnace nucleation plus laser growth HT, and for the first time demonstrates a technique that predicts the structural changes associated with formation of the crystalline phase(s) responsible for an effective refractive index change which yields a GRIN optical element. In this study the

refractive index change upon a ceramization in $15\text{GeSe}_2\text{-}45\text{As}_2\text{Se}_3\text{-}40\text{PbSe}$ was shown to be directly related to the growth of crystals inside of the glassy matrix. A calculated effective index from XRD data was shown to agree with experimentally measured refractive index of the samples. Refractive index change upon a ceramization was also shown to be directly correlated to changes in the Raman spectrum and therefore crystal growth. A Raman ratio was defined which could be correlated to the refractive index, and allows for indirect verification of spatially varying structural modification that correlates with spatially varying refractive index modification. Laser-induced heating via highly absorbing bandgap irradiation was used to create a temperature profile throughout the volume of a sample, inducing a gradient in growth rate of pre-nucleated crystal phases. The Raman ratio was then measured on a cross-section, to predict the thermal profile seen by the sample under irradiation and determine its resulting estimated GRIN profile. Optical functionality through focusing was demonstrated as a result of employing the laser-induced heating profile on a pre-nucleated glass specimen, validating this approach to forming 3-D GRIN structures. Such ability to spatially vary, model and quantify the nanocrystallization process possible in candidate GRIN materials will enable new advances in novel GRIN materials for infrared optical applications.

Funding

Defense Advanced Research Projects Agency (FA8650-12-C-7225).

Acknowledgments

This work was supported in part by the Defense Advanced Research Projects Agency under Air Force Research Laboratory contract FA8650-12-C-7225 through the M-GRIN Tech Area 2 program, and has been approved for public release, distribution unlimited. The views, opinions and/or findings expressed are those of the authors and should not be interpreted as representing the official views or policies of the Department of Defense or the U.S. Government.

The authors acknowledge the helpful insight from discussions with Professor Edgar Zanotto, as well as those with collaborator Alexej Pogrebnjakov at Penn State University related to the goals of this work.